Ocean Modelling 205 (2027) 102817

Contents lists available at ScienceDirect

Ocean Modelling

journal homepage: www.elsevier.com/locate/ocemod

Numerical study on genesis of wintertime low sea level anomaly off northwestern Luzon and dominant factor in super-ENSO-related changes

Tzu-Ling Chiang [a], Yi-Chia Hsin [a,b,*], Chau-Ron Wu [a,b,c,*]

[a] Research Center for Critical Issues, Academia Sinica, Tainan, Taiwan
[b] Research Center for Environmental Changes, Academia Sinica, Taipei, Taiwan
[c] Department of Earth Sciences, National Taiwan Normal University, Taipei, Taiwan

ARTICLE INFO

Keywords:
Low sea level anomaly
Northwestern Luzon
El Niño-Southern Oscillation
South China Sea model

ABSTRACT

Satellite remote sensing altimetry data have demonstrated that wintertime low sea level anomaly off northwestern Luzon (NWL-SLA) is a common feature. The genesis of the wintertime low NWL-SLA and its response to the most recent two super El Niño-Southern Oscillation (ENSO) in 1997–1998 and 2015–2016 are explored by conducting a series of numerical experiments based on a well-validated three-dimensional South China Sea (SCS) model. Our analysis emphasizes that the generation of low NWL-SLA and its super-ENSO-related variability are triggered by different dynamical processes. The wintertime local positive wind stress curl off northwestern Luzon serves as the primary driver of low NWL-SLA formation. However, remote signals originating in the tropical western Pacific Ocean represent the dominant source to regulate the super-ENSO-related changes in NWL-SLA, rather than the variabilities of local wind stress curl and ocean currents in the vicinity of Luzon Strait. These remote signals originate from the baroclinic component of sea level changes and propagate westward at speeds of the first-mode baroclinic Rossby wave; subsequently, they enter the SCS clockwise through the southernmost gap of Sibutu Passage and Mindoro Strait at speeds of the baroclinic coastal Kelvin wave. Furthermore, faster wave propagation speeds are observed during La Niña years than El Niño years because of the greater reduced gravity associated with stronger stratification during La Niña years.

1. Introduction

The northern South China Sea (SCS), particularly in the region off northwestern Luzon (hereafter NWL, defined by the white frame in Fig. 1; 117.5°E-121°E, 16.5°N-20°N), has been suggested to be characterized by a prominent low sea level anomaly (SLA) in winter (Shaw and Chao, 1994; Shaw et al., 1999; Qu, 2000; Liu et al., 2008). This low SLA is often associated with the cyclonic circulation driven by the northeasterly winter monsoon or cold-core cyclonic eddy known as the Luzon Cold Eddy or West Luzon Eddy (Shaw and Chao, 1994; Qu, 2000; Wu and Chiang, 2007; Liu et al., 2008). Understanding the dynamics governing the formation and variability of this low SLA is crucial, as it fundamentally regulates the regional ocean circulation, sea level (SL) gradients, and upper-ocean thermal structures in the northern SCS, further influencing regional climate and biogeochemistry (Liu et al., 2002; Xie et al., 2003; Isoguchi and Kawamura, 2006; Voss et al., 2006; Zhao and Tang, 2007; Hein et al., 2013; Kämpf and Chapman, 2016; Xiao et al., 2018, 2019, 2020a, 2020b; Ngo and Hsin, 2021; Umasangaji and Ramili, 2021, 2024). In addition to its pronounced seasonal lifecycle, the wintertime low NWL-SLA exhibits significant interannual variability that is closely tied to the El Niño-Southern Oscillation (ENSO) (Wu et al., 1998; Wu and Chang, 2005). Wu and Chang (2005) identified unusual warming and positive SLA in the NWL during the winter of 1998. However, the exact processes leading to these dramatic SL fluctuations during super ENSO events remain to be fully elucidated.

To clarify super-ENSO-related changes in the wintertime low NWL-SLA, we first examine whether mean wintertime sea level can respond consistently to "super ENSO" (defined by Oceanic Niño Index > 2 °C; Chen et al., 2017; Santoso et al., 2017) based on the Data Unification and Altimeter Combination System (DUACS) satellite altimeter gridded absolute dynamic topography (ADT). Here, "super ENSO" is used to express a complete super ENSO cycle, which is defined as the progression from a normal pre-El Niño year, through a super El Niño year (Oceanic Niño Index > 2 °C), and subsequently to a super La Niña year (Oceanic Niño Index < −2 °C).

* Corresponding author at:
E-mail addresses: ychsin@as.edu.tw (Y.-C. Hsin), cwu@ntnu.edu.tw (C.-R. Wu).

https://doi.org/10.1016/j.ocemod.2026.102817
Received 7 September 2025; Received in revised form 27 August 2026; Accepted 27 August 2026
Available online 29 August 2026

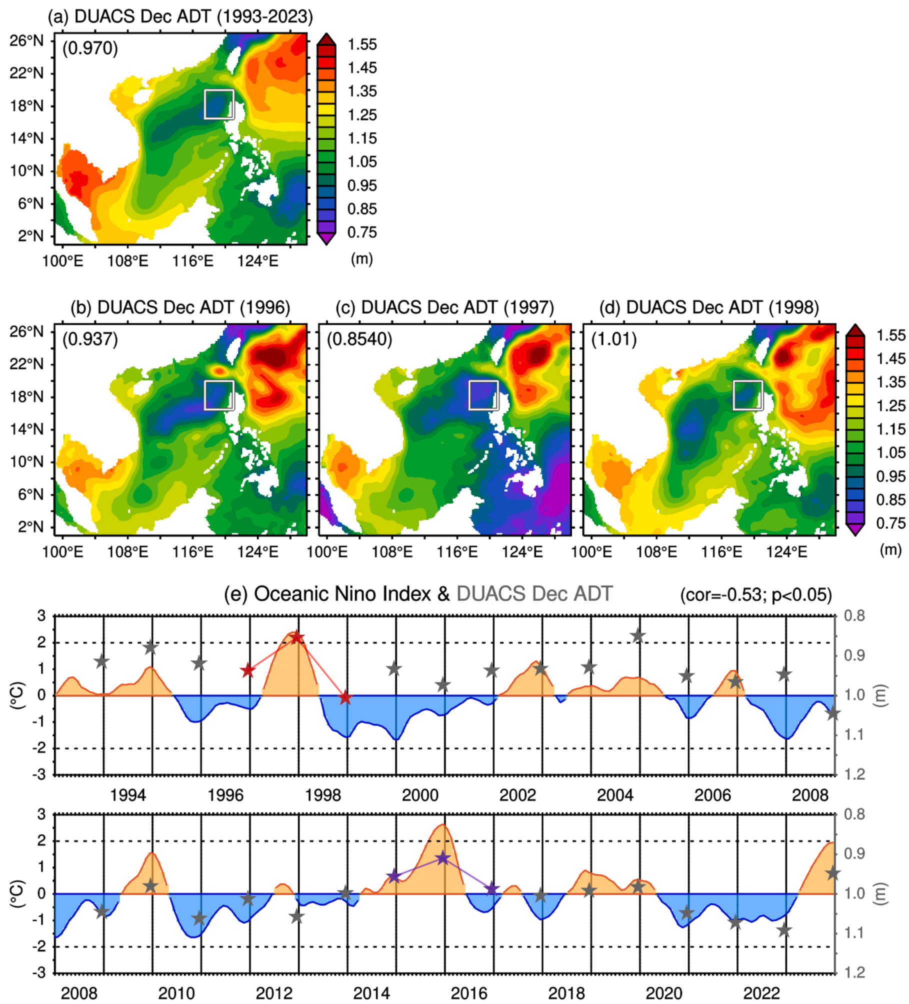

Fig. 1. (a) Climatological December mean absolute dynamic topography (ADT; unit: m) averaged over 1993–2023. Horizontal distributions of December mean ADT (unit: m) in (b) 1996, (c) 1997, and (d) 1998. (e) Time series of monthly Oceanic Niño Index (ONI; unit: °C https://www.cpc.ncep.noaa.gov/products/analysis_monitoring/enso/oni/v5/; curve) versus the December mean ADT averaged in the NWL (star; NWL-ADT). The ADT is obtained from the Data Unification and Altimeter Combination System (DUACS). The NWL-ADT is the ADT averaged over the white-outlined box and ADT on grid with bottom topography $<$ 500 m is excluded in the calculation. The values in the upper-left corner of (a)-(d) indicate the corresponding NWL-ADT.

On the climatological December mean ADT map (Fig. 1a), low ADT anomaly is apparent in the NWL. As focused on the most recent two super ENSO events of 1997–1998 and 2015–2016, the ADT fluctuation follows a ranking as medium during normal years, low during El Niño years, and high during La Niña years, i.e., lower in December 1997/2015 (super El Niño years; Fig. 1c and S1b) and higher in December 1998/2016 (super La Niña years; Fig. 1d and S1c) compared to December 1996/2014 (normal pre-El Niño years; Fig. 1b and S1a) and the climatological December average (Fig. 1a). This ranking order held true from November but was disrupted in January (figure not shown).

The present study focuses on clarifying the dynamical processes underlying the wintertime low NWL-SLA, including its formation mechanism and response to super ENSO of 1997/1998 and 2015/2016 when the Oceanic Niño Index reached extraordinary amplitudes greater than 2 °C in the central equatorial Pacific Ocean (Chen et al., 2017; Santoso et al., 2017) and had great socioeconomic impacts (Bouma et al., 1997; McPhaden et al., 2006; Chen et al., 2015). Several competing mechanisms have been proposed regarding the genesis and interannual modulations of the NWL-SLA. On one hand, local atmospheric forcing, specifically the basin-scale or local positive wind stress curl (WSC) associated with the northeasterly winter monsoon, has been widely reported as a primary driver of the seasonal cyclonic circulation and the subsequent depression of sea level in the northern SCS (Chao et al., 1996; Qu, 2000). On the other hand, remote oceanic processes originating from the Pacific Ocean are argued to exert dominant controls on the interannual timescales (Zheng et al., 2007; Wu, 2013; Zhuang et al., 2013; Li et al., 2021). Zheng et al. (2007) attributed the interannual SLA off northwestern Luzon to variations in the Kuroshio intrusion through the Luzon Strait and the associated Luzon Strait transport (LST), which can directly modulate the upper-ocean thermal structure and regional sea surface height gradients via geostrophic adjustments and vorticity injections. Wu (2013) further connected the interannual LST with North Equatorial Current bifurcation latitude and showed that the influence of the ENSO on the Kuroshio intrusion and SLA off northwestern Luzon is significant only during Pacific Decadal Oscillation (PDO) cold phase. Conversely, Zhuang et al. (2013) suggested another pathway toward the opposite direction based on a wave-interconnection mechanism: Pacific basin winds excite low-frequency baroclinic Rossby waves, which trigger coastal Kelvin waves to travel clockwise along the Philippine coast. These waves propagate into the Sulu Sea and eastern SCS, thereby modulating the regional SLA on interannual-to-decadal scales. Recently, Li et al. (2021) also verified that the Mindoro-Sibutu pathway acts as a critical conduit for transferring multi-layer circulation signals between the western Pacific Ocean and the SCS.

Despite these insights, a systematic differentiation between the

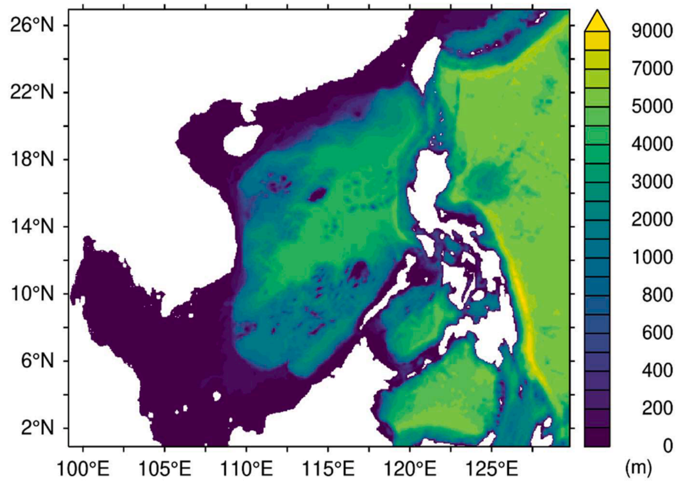

Fig. 2. The bathymetry (unit: m) of SCSM.

factors responsible for the basic genesis of the low NWL-SLA and the drivers of its super-ENSO-related variations has been lacking. To bridge this gap, the main objective of this study is to investigate the detailed dynamical processes and pathways controlling the NWL-SLA under super-ENSO-induced forcing based on a well-validated three-dimensional South China Sea model (SCSM) through five groups of numerical experiments. The remainder of this paper is organized as follows. Section 2 briefly describes the data and SCSM. Section 3 thoroughly investigates the genesis of the wintertime low NWL-SLA. Section 4 examines the mechanisms driving super-ENSO-related NWL-SLA. Section 5 provides the discussion of the inconsistency between the NWL-SLA and vertical velocity variation during super ENSO. Section 6 concludes the main findings.

2. Data and model

2.1. Satellite altimeter data and Oceanic Niño Index

The absolute dynamic topography (ADT) used in this study is obtained from Data Unification and Altimeter Combination System (DUACS) satellite-altimeter gridded sea surface height dataset. This product (https://doi.org/10.48670/moi-00148) is processed by the DUACS multimission altimeter data processing system, in which satellite-altimeter gridded ADT is computed with respect to the mean of 1993–2012, and estimated by Optimal Interpolation, merging the L3 along-track measurements from the different altimeter missions available. The DT2024 version with a horizontal resolution of 0.125° and a temporal interval of one day in 1993–2023 is adopted.

The index used to present the occurrence of ENSO is the Oceanic Niño Index (ONI; https://www.cpc.ncep.noaa.gov/products/analysis_monitoring/enso/oni/v5/) provided by Climate Prediction Center, National Oceanic and Atmospheric Administration (NOAA). Based on the Extended Reconstructed Sea Surface Temperature version 5 (ERSST.v5) dataset, the ONI is 3 month running mean of sea surface temperature anomaly averaged in the Niño 3.4 region (5°N-5°S, 120°W-170°W), based on centered 30-year base periods updated every 5 years. The ONI uses a three-month running average to make it more stable for determining El Niño/La Niña events and avoid the impact of anomalous fluctuations from single month on the assessment.

2.2. South China Sea model

Based on the Princeton Ocean Model (Mellor, 2004), we have built up the SCSM with a domain covering the entire SCS basin and part of the western Philippine Sea. The SCSM has a resolution of 1/20° with a domain extending from 99°E to 130°E in longitude and from 1°N to 27°N in latitude (Fig. 2), and 26 sigma levels in the vertical. This model is upgraded from Wu and Chiang (2007) and Chiang et al. (2008, 2011). At the open boundaries of the SCSM, sea surface height, velocity, temperature, and salinity are specified from the daily output of a global data assimilation product, the 1/12° global Hybrid Coordinate Ocean Model (HyCOM; https://www.hycom.org/). At the sea surface, the SCSM is forced by 6-hourly wind stress, daily sea surface temperature, and daily heat fluxes obtained from the fifth generation European Centre for Medium-Range Weather Forecasts (ECMWF) atmospheric reanalysis (ERA5) of global climate (Copernicus Climate Change Service, 2017; Hersbach et al., 2020). Initialized from the sea surface height, temperature, salinity, and velocity data of HyCOM on January 1, 1994, the SCSM is spun up for one year. Sequentially, the SCSM is run for the period 1995–2023, and the daily output is used for analysis in the present work. This simulation is hereafter named as Control Run (CTL).

Validations with observed temperature from a long-term mooring station in the northern SCS (SouthEast Asian Time-series Study station; SEATS) and flow velocity from two mooring stations in the SCS have also

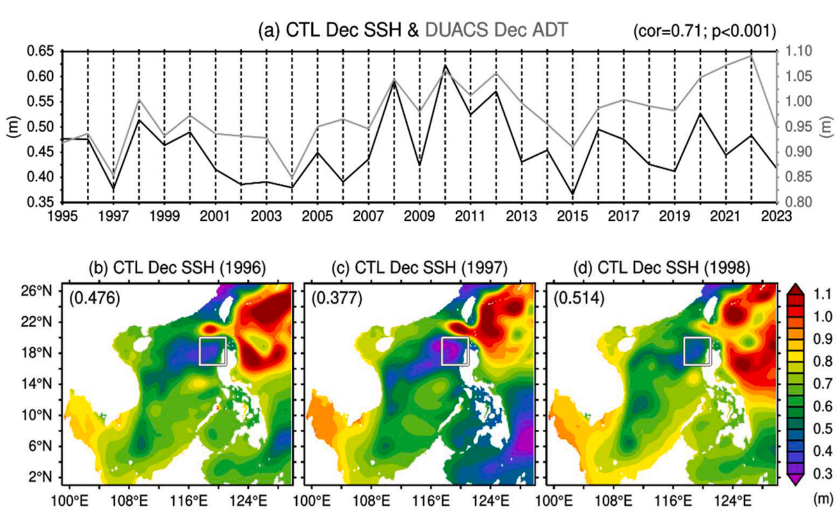

Fig. 3. (a) Time series of December mean sea surface height (SSH; unit: m) derived from the CTL (black) versus December mean absolute dynamic topography (ADT; unit: m) of DUACS (gray) during the period of 1995–2023, and horizontal distributions of CTL-simulated December mean SSH in (b) 1996, (c) 1997, and (d) 1998. In (a), the SSH and ADT are area-averaged over the NWL (white-outlined box in b-d). In (b)-(d), the values in the upper-left corner represent the area-averaged SSH over the NWL.

Table 1
Summary of group 1 numerical experiments.

Group	Case Name	Wind	Lateral Boundary Condition (LBC)
1	ClmDec	Climatological December average over 1995–2023 (CLM-DEC)	CLM-DEC
	NoWind	wind stress = 0	
	NoWSC	Homogeneous northeasterly at wind stress of 0.1 N/m^2	

been repeated for the CTL as done by Wu and Chiang (2007). Then, comparisons between the CTL and DUACS are also performed for sea level, the target variable of the present study. The spatial pattern correlation coefficients for the annual march of climatological monthly sea level distribution in the SCS are greater than 0.96 (Figure S2) and those for monthly sea level distribution during 1995–2023 range between 0.79 and 0.94 with a mean of 0.91±0.03 (Figures S2 and S3). The time series of simulated December mean modeled sea surface height variability averaged over the NWL generally reflects the December remotely sensed NWL-ADT for the period 1995–2023, with a correlation coefficient of 0.71, especially for the two super ENSO of 1997–1998 and 2015–2016 (Fig. 3a). The spatial distributions of super-ENSO-related changes in NWL-SLA are also well reproduced by the CTL, with high spatial pattern correlation coefficients of 0.91–0.96 (red stars in Figure S3). The SCSM consistently reproduces not only the mean state but also the interannual variability, thereby demonstrating the model's reliability in capturing super-ENSO-induced anomalies (Figures S4 and 3b-3d). All validation results support the suitability of the SCSM in the study and demonstrate that the model is well-suited for elucidating the underlying mechanisms governing super-ENSO-related changes in the NWL-SLA.

Besides the CTL, five groups of additional experiments (39 experiments in total) are designed to further elucidate the roles of winds inside or outside the SCS in controlling NWL formation and to identify the dominant factors underlying super-ENSO-related changes in the NWL-SLA. For consistency and simplification, all experiments in the five groups are initialized from climatological December mean conditions (long-term average over the period of 1995–2023; hereafter DEC) for SSH, temperature, salinity, and velocity from HyCOM, and are forced by climatological DEC sea surface temperature and heat fluxes from ERA5 at the air-sea interface. The experiments differ in their wind fields and open boundary conditions according to the specific objectives of each group. All experiments require at least three months to spin up from the climatological DEC initial conditions (figure not shown), and their simulation duration is adjusted based on the requirements of each group. Details of each experiment are provided in the following sections where they are discussed.

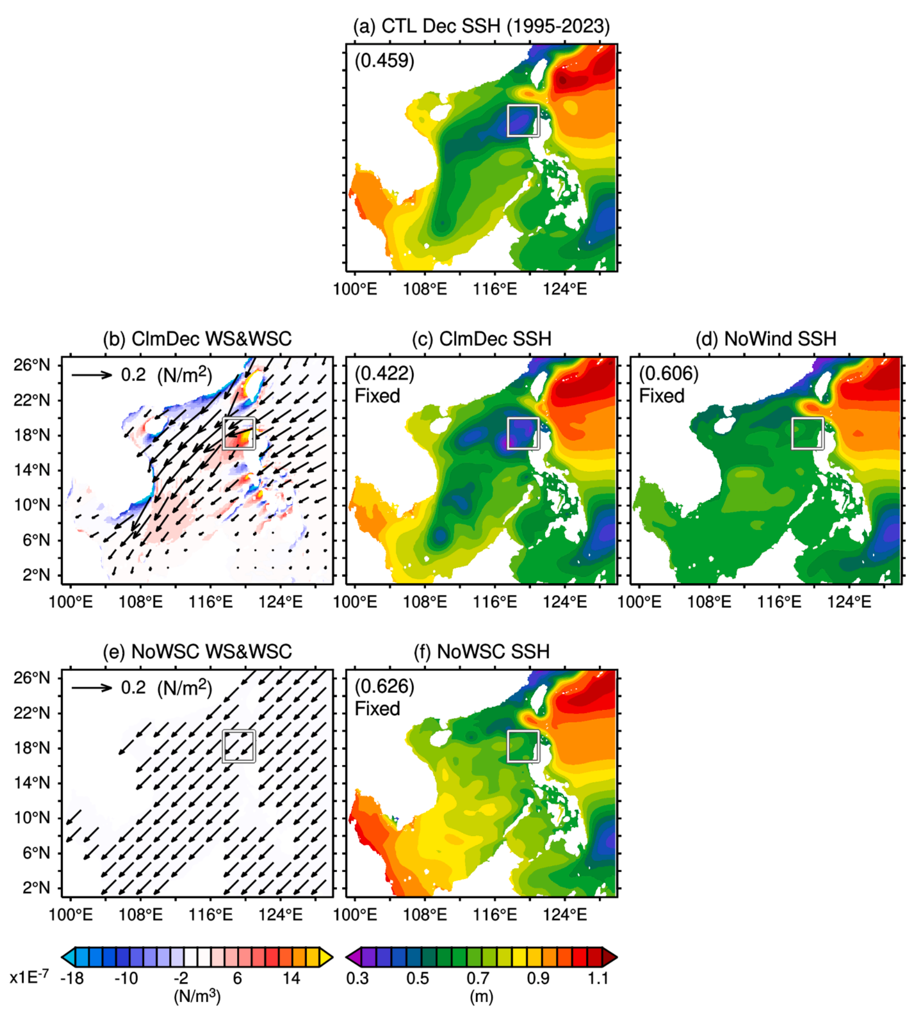

Fig. 4. Wind fields and simulated SSHs for the experiments of Group 1. (a) Climatological December mean SSH over 1995–2023 simulated by the CTL. (b, c) Wind field and simulated SSH for ClmDec. (d) simulated SSH for NoWind. (e, f) Wind field and simulated SSH for NoWSC. In Group 1, simulations are run for one year and the averages of the last two months are plotted to remove high-frequency noises. The values in the upper-left corner of SSH plots represent the area-averaged SSH over the NWL (white-outlined box). Units of WS, WSC, and SSH are N/m^2, N/m^3, and m, respectively.

Table 2
Summary of Groups 2 and 3 numerical experiments.

Group	Case Name	Wind	Lateral Boundary Condition (LBC)
2	WB96d	December mean (DEC) of 1996	DEC of 1996
	WB97d	DEC of 1997	DEC of 1997
	WB98d	DEC of 1998	DEC of 1998
3	**W96B96**	6-hourly wind in July-December (6HR) of 1996	Daily HyCOM in July-December (DHyCOM) of 1996
	W97B96	6HR of 1997	
	W98B96	6HR of 1998	
	W96B97	6HR of 1996	DHyCOM of 1997
	W97B97	6HR of 1997	
	W98B97	6HR of 1998	
	W96B98	6HR of 1996	DHyCOM of 1998
	W97B98	6HR of 1997	
	W98B98	6HR of 1998	

3. Genesis of low NWL-SLA

Shaw et al. (1996) first proposed that the wintertime low NWL-SLA is driven by remote forcing from SCS basin-scale circulation rather than local offshore Ekman transport induced by southward wind stress (WS) along the western coast of Luzon. Subsequent studies suggested that basin-wide positive WSC in the SCS serves as the primary driving force for low NWL-SLA formation (e.g., Chao et al., 1996; Chu et al., 1998; Qu, 2000; Liu et al., 2002; Martin and Villanoy, 2007; Wang et al., 2010; Lu et al., 2015; Hu and Wang, 2016). To identify the respective roles of WS and WSC in generating the low NWL-SLA, we conducted three experiments (Group 1 in Table 1). Each experiment was run for one year, with outputs from the final two months used for analysis.

Driven by the climatological December wind field (see wind pattern in Fig. 4b), the first experiment (ClmDec) is conducted to determine whether December wind alone can establish the basic features of the wintertime SCS sea level distribution. In this simulation, a typical wintertime SSH pattern is reproduced (cf. Fig. 4a and c). Subsequently, the typical basin-wide SSH pattern fails to develop and the SSH off western Luzon rises significantly in both the NoWind experiment (Fig. 4d), where the wind is set to zero, and NoWSC experiment (Fig. 4f), which is driven by a homogeneous northeasterly wind field with a magnitude of 0.1 N/m^2 (i.e., no WSC; see wind pattern in Fig. 4e). Thus, we can conclude that the low NWL-SLA is generated by the WSC directly rather than by the WS or the Luzon Strait transport, and the local positive WSC west of Luzon is the main driver.

4. Mechanisms underlying super-ENSO-related changes in the low NWL-SLA

To elucidate how the low NWL-SLA responds to super ENSO, we performed four groups of experiments (Groups 2–5) using the three

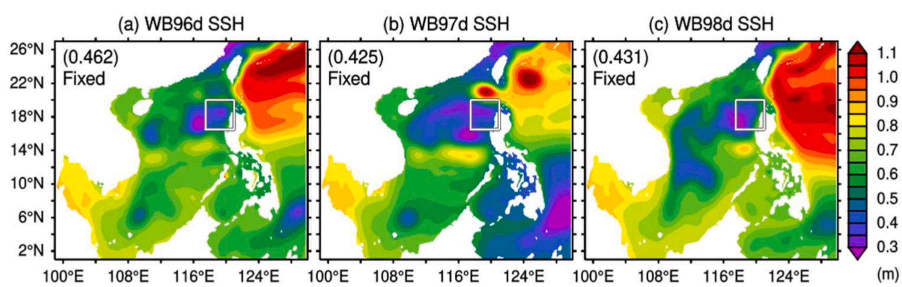

Fig. 5. Simulated SSH (unit: m) in the experiments of Group 2. (a) WB96d, (b) WB97d, and (c) WB98d. Experiments are run for one year and the averages of the last two months are plotted to remove high-frequency noises. The values in the upper-left corner of SSH plots represent the area-averaged SSH over the NWL (white-outlined box).

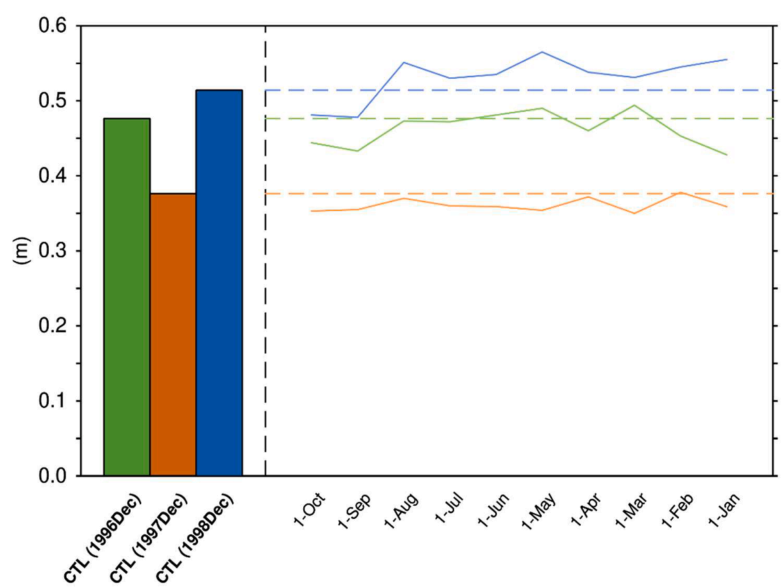

Fig. 6. December NWL-SSH (unit: m) simulated by (bars left of the black dashed line) the CTL (green: 1996; orange: 1997; blue: 1998) and (curves right of the black dashed line) the experiments of W96B96 (green), W97B97 (orange), and W98B98 (blue) with variant starting dates from 1-October to 1-January in the corresponding year.

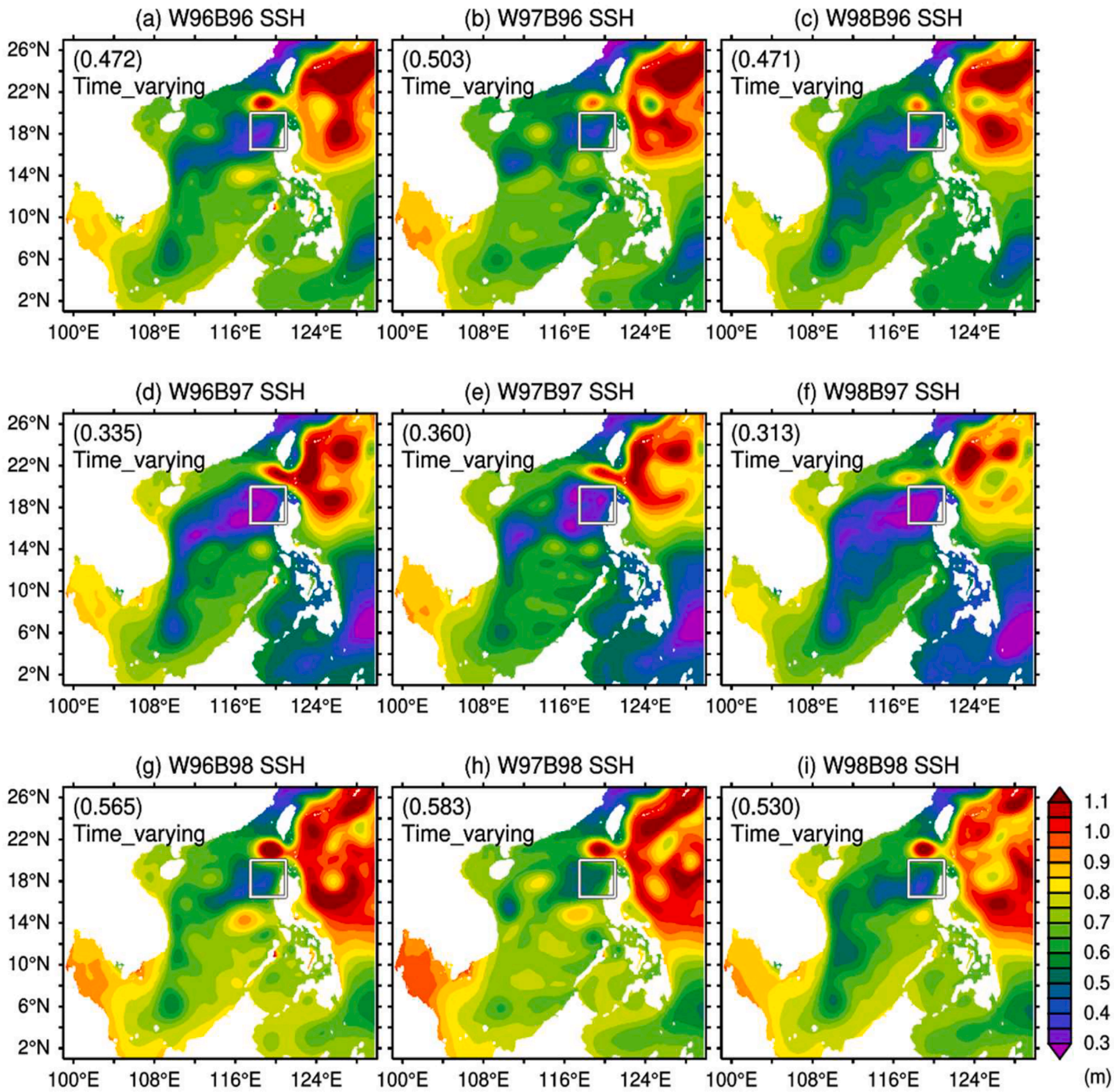

Fig. 7. December mean SSH (unit: m) simulated by the experiments of Group 3. (a) W96B96, (b) W97B96, (c) W98B96, (d) W96B97, (e) W97B97, (f) W98B97, (g) W96B98, (h) W97B98, and (i) W98B98. The values in the upper-left corner of SSH plots represent the area-averaged SSH over the NWL (white-outlined box).

Table 3
Summary of Group 4 numerical experiments.

Group	Case Name	Wind	Lateral Boundary Condition (LBC)
4	W96B**cd**	6-hourly wind in July-December (6HR) of 1996	Climatological December mean averaged over 1995–2023 (CLM-DEC)
	W97B**cd**	6HR of 1997	CLM-DEC
	W98B**cd**	6HR of 1998	CLM-DEC
	WyyBcd**N**yy	Same as WyyBcd, but daily HyCOM (DHyCOM) of the corresponding year at **northern** boundary; yy=96, 97, or 98	
	WyyBcd**E**yy	Same as WyyBcd, but DHyCOM of the corresponding year at **eastern** boundary; yy=96, 97, or 98	
	WyyBcd**S**yy	Same as WyyBcd, but DHyCOM of the corresponding year at **southern** boundary; yy=96, 97, or 98	

years of 1996–1998, where 1996, 1997, and 1998 represent normal pre-El Niño, super El Niño, and super La Niña conditions, respectively. As described in the Introduction, December NWL-SLA ranked as medium (0.937 m), low (0.854 m), and high (1.005 m) for 1996, 1997, and 1998, respectively (Fig. 1b-d). Therefore, we adopted this specific ranking pattern of December sea-level changes among the three years as the criterion for determining whether super-ENSO-related NWL-SLA is properly reproduced in our numerical experiments.

4.1. Is wind the key factor resulting in the super-ENSO-related changes in NWL-SLA?

Previous research has identified two potential factors driving ENSO-related NWL-SLA: local wind forcing within the SCS that affects basin-scale circulation, and remote wind forcing in the Pacific basin that influences Kuroshio variability or wave motion in the northwestern Pacific Ocean (Wu and Chang, 2005; Zheng et al., 2007; Zhuang et al., 2013). Forced by mean wind forcing and lateral boundary conditions of December-1996, December-1997, and December-1998, respectively, the Group 2 experiments (WB96d, WB97d, and WB98d; Table 2) are designed to examine whether constant December forcing of the three years alone can generate super-ENSO-related NWL-SL changes. Although these experiments successfully reproduced typical basin-scale SSH pattern (Fig. 5), the simulated SSH in the NWL (NWL-SSH) followed an incorrect ranking of high (0.462 m), low (0.425 m), and medium (0.431 m) for WB96d, WB97d, and WB98d, respectively, instead of the

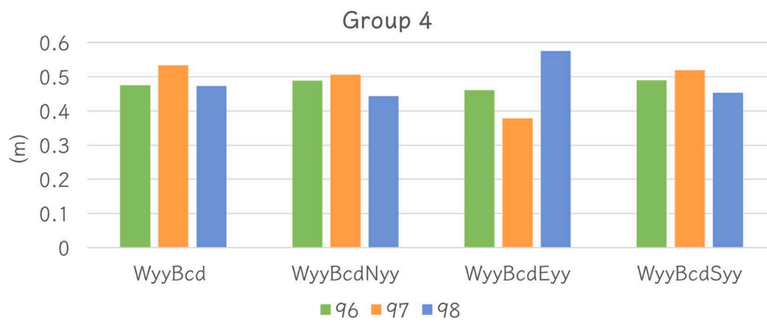

Fig. 8. December NWL-SSH (unit: m) simulated by Group 4 experiments.

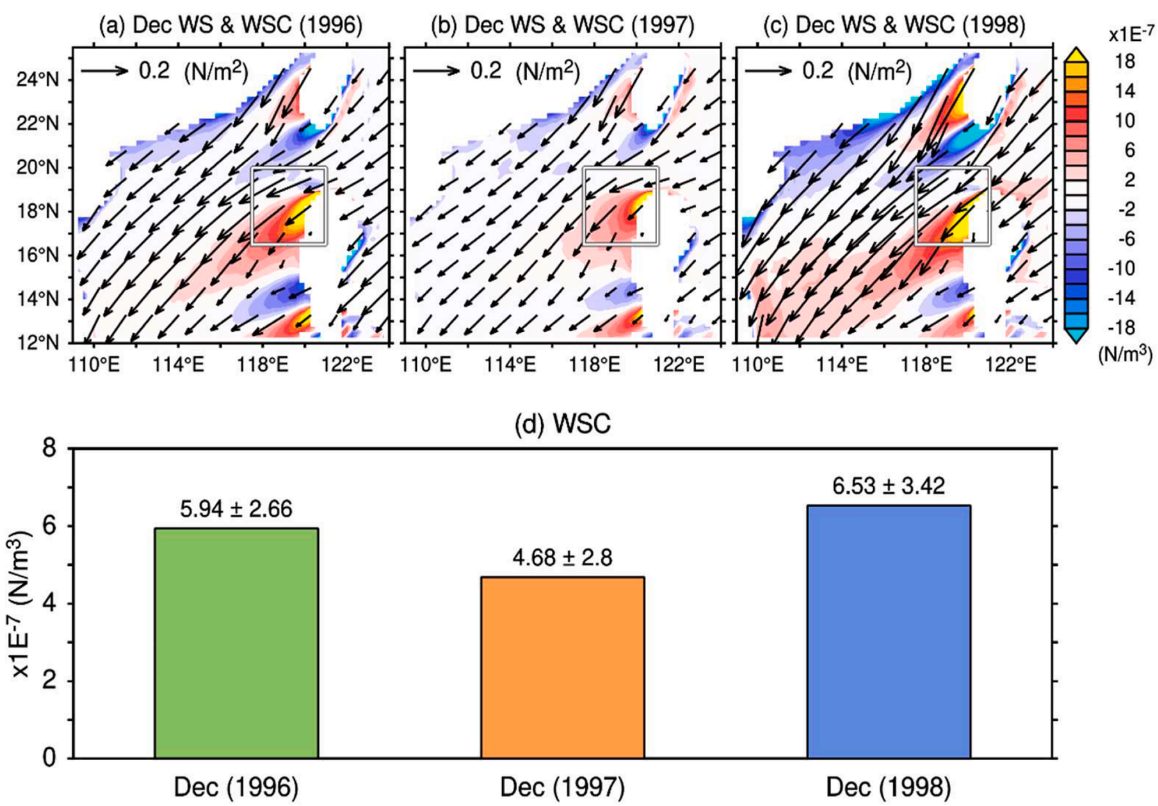

Fig. 9. December mean wind stress (WS; vectors; unit: N/m^2) and wind stress curl (WSC; shading; unit: N/m^3) in the vicinity of the NWL (white-outlined box) in (a) 1996, (b) 1997, and (c) 1998, and (d) Comparison of December mean WSC over the NWL among 1996 (green), 1997 (orange), and 1998 (blue). According to the t-test results, all pairwise differences among the three years are statistically significant ($p < 0.001$). The hourly wind data used for the calculation of WS and WSC is obtained from the ECMWF-ERA5.

Table 4
Summary of Group 5 numerical experiments.

Group	Case Name	Description
5	WyyBcdEyy-SSH	Same as WyyBcdEyy, but velocity, temperature, and salinity (UVST) of CLM-DEC and SSH of DHyCOM in corresponding year at **eastern** boundary; yy=96, 97, or 98
	WyyBcdEyy-UVST	Same as WyyBcdEyy, but UVST of DHyCOM in corresponding year and SSH of CLM-DEC at **eastern** boundary; yy=96, 97, or 98
	WyyBcdEyy-SSHbt	Same as WyyBcdEyy-SSH, but barotropic SSH of DHyCOM in corresponding year at **eastern** boundary; yy=96, 97, or 98
	WyyBcdEyy-SSHbc	Same as WyyBcdEyy-SSH, but baroclinic SSH of DHyCOM in corresponding year at **eastern** boundary; yy=96, 97, or 98

expected medium, low, and high sequence. That is, constant December forcing cannot accurately drive super-ENSO-related NWL-SL changes. Thus, the atmospheric and oceanic forcing responsible for these variations should be time-varying rather than temporally uniform.

To demonstrate the necessity of time-varying forcing, W96B96, W97B97, and W98B98 (Group 3; Table 2) were driven by time-varying 6-hourly wind fields and daily lateral boundary conditions from the corresponding years of 1996, 1997, and 1998, respectively. Sensitivity tests using different model initialization dates (e.g., 1-December, 1-November, 1-October, etc.) were done to ensure how long the experiments need to be spun up, and revealed that the December NWL-SSH ranking among the three experiments (medium, low, and high for normal, El Niño, and La Niña years, respectively) stabilizes once the SCSM runs for longer than 5 months, i.e., starting on 1-August (Fig. 6). Thus, Group 3 experiments were run for the period of July-December. Because the correct ranking of NWL-SSH can be reproduced by the

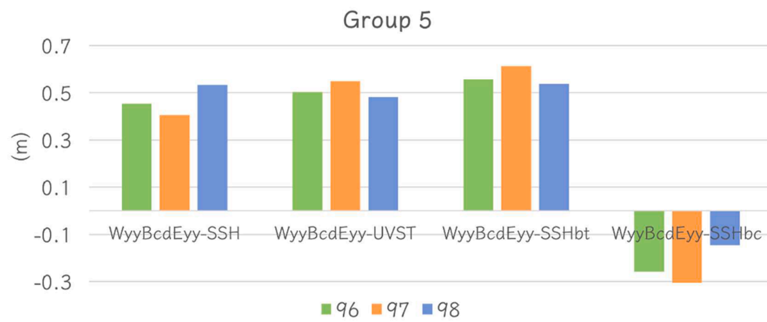

Fig. 10. December NWL-SSH (unit: m) simulated by Group 5 experiments.

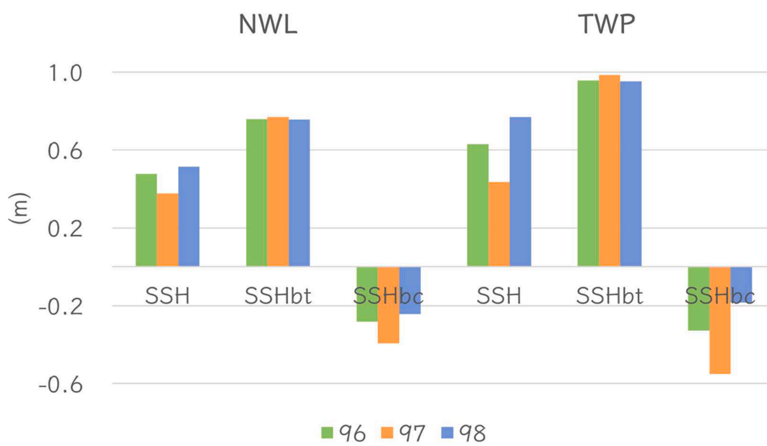

Fig. 11. Comparison of SSH components (SSH, SSHbt, and SSHbc; unit: m) in the NWL and the tropical western Pacific (TWP; 128°E-130°E, 3°N-17°N) for the 1996–1998. The SSH is based on the CTL simulation.

three experiments (Fig. 7a, e, and i), it indicates that time-varying forcing is essential for reproducing super-ENSO-related sea-level variations.

4.2. Is the super-ENSO-related NWL-SLA driven by the local wind or remote wind?

In Group 3 experiments (Table 2), we use cross-combinations of time-varying wind forcing (WF) and time-varying lateral boundary conditions (LBC) on the basis of W96B96, W97B97, and W98B98 to clarify the relative importance of local and remote forcing in governing super-ENSO-related NWL-SLA. Here, WF and LBC can be generally considered as local and remote forcing, respectively. Since the generation of the low NWL-SLA has been attributed to local positive WSC off the northwestern Luzon in Section 3 of this study, it is worth to first examine whether local WSC also dominates low NWL-SLA during super ENSO. To address this question, we compare experiments with identical LBC but different WF: specifically, W96B96 versus W97B96/W98B96, W97B97 versus W96B97/W98B97, and W98B98 versus W96B98/W97B98. If local wind effectively drives super-ENSO-related NWL-SLA, the simulated December NWL-SSH should exhibit medium, low, and high values in 1996, 1997, and 1998, respectively, when the same LBC is applied (i.e., B96, B97, or B98).

When LBCs in 1996 (i.e., B96) are applied, the general SCS SSH pattern is well reproduced, including the basin-wide SSH and the NWL-SSH. However, the values of NWL-SSH in the experiments of W96B96 (0.472 m; medium), W97B96 (0.503 m; high), and W98B96 (0.471 m; low) do not follow the expected ranking of medium, low, and high values (Fig. 7a-c). Similarly, the rankings for NWL-SSH in the other two experimental sets with 1997 and 1998 LBCs (B97 and B98) also fail to match the expected order (cf. Fig. 7d-f and g-i). These results indicate that interannual changes in local wind forcing do not contribute significantly to super-ENSO-related NWL-SL variations.

Experiments with the same WF but different LBCs from 1996, 1997, and 1998 (i.e., W96, W97, and W98) are compared to assess the role of remote forcing originating from outside the SCSM domain. When the WF is fixed to 1996, the experiments W96B96, W96B97, and W96B98 generate the correct ranking of December NWL-SSH: medium (0.472 m), low (0.335 m), and high (0.565 m) from 1996 to 1998, respectively (Fig. 7a, d, and g). The same NWL-SSH ranking is reproduced when WF is fixed to 1997 and 1998 (cf. Fig. 7b, e, and h and Fig. 7c, f, and i), showing a consistent response of NWL-SSH to super-ENSO-related variability through remote forcing from outside the SCS. This outcome is also valid for the most recent super ENSO of 2015–2016 (see Figure S5 in the supplement).

4.3. Where is the origin of remote forcing?

Group 4 experiments were designed to determine which open boundary of the SCSM serves as the entry point for remote forcing. Since LBCs represent remote forcing in our model setup, we first established baseline cases by replacing the time-varying LBCs in W96B96, W97B97, and W98B98 with **C**limatological **D**ecember averages (CLM-DEC) at the northern, eastern, and southern boundaries (creating W96B**cd**, W97B**cd**, and W98B**cd**; Table 3). This configuration eliminates time-varying remote signals, allowing local wind variations to regulate NWL-SSH changes. The values of NWL-SSH in W96Bcd (0.475 m), W97Bcd (0.534 m), and W98Bcd (0.473 m) are higher in 1997 with comparable values in the other two years (Fig. 8), corresponding to local WSC changes observed in Decembers of 1996, 1997, and 1998 (Fig. 9). Then, we reintroduced time-varying LBCs of the corresponding year at individual open boundaries (northern, eastern, or southern) to determine

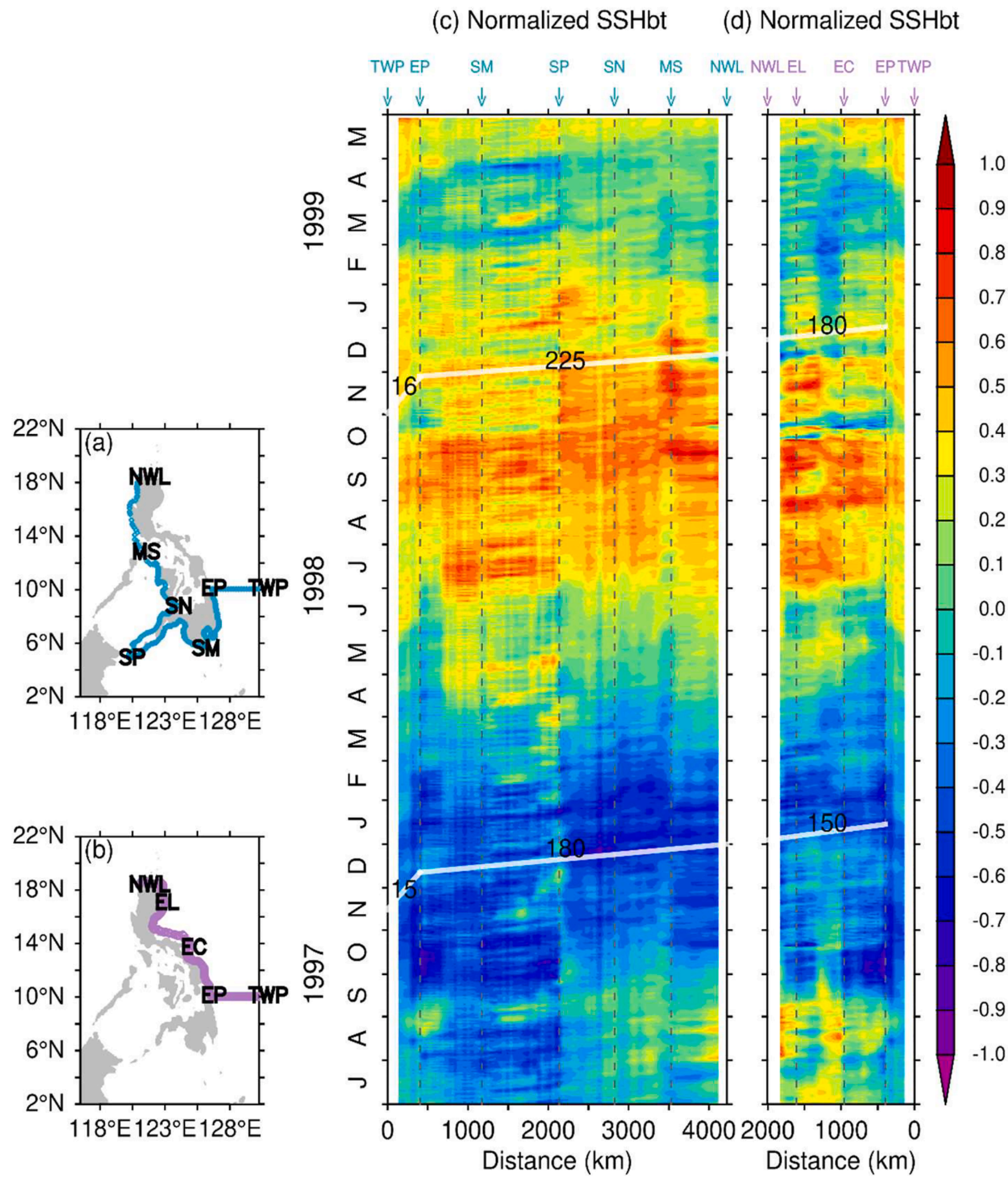

Fig. 12. Routes in (a) blue and (b) purple color used to trace the baroclinic wave motion from the tropical western Pacific (TWP) to the NWL. EP, SM, SP, SN, MS, EC, and EL are the primary nodes along the two routes. (c, d) Hovmöller diagrams for the 1997–1998 super ENSO showing the temporal evolution of SSHbc anomaly normalized by 3 times of standard deviation from the TWP to NWL along the blue and purple routes, respectively. The white lines in (c) and (d) show the propagation of baroclinic waves during the winters of 1997 and 1998, and values next to the white lines are the estimated wave propagation speeds (unit: km/day) for each segment. (EP: East of Philippines; SM: South of Mindanao; SP: Sibutu Passage; SN: South of Negros; MS: Mindoro Strait; EC: East of Catanduanes; EL: East of Luzon).

the primary entry pathway for remote signals. As revealed in Fig. 8, only experiments with time-varying LBCs set at the eastern boundary (W96BcdE96, W97BcdE97, and W98BcdE98) can successfully reproduce the expected ranking of NWL-SSH: medium, low, and high. This result demonstrates that super-ENSO-related signals originate from the western Pacific Ocean, echoing the results of Zheng et al. (2007), Zhuang et al. (2013), and Li et al. (2021).

To examine whether the super-ENSO-related NWL-SSH anomalies are driven by wave or current motions, respectively, we conducted the following sensitivity experiments. In these runs, either time-varying or CLM-DEC LBCs are applied to the SSH and other variables at the eastern boundary of the SCSM (WyyBcdEyy-SSH and WyyBcdEyy-UVST; Table 4). The correct ranking of NWL-SSH is obtained in experiments of WyyBcdEyy-SSH (Fig. 10), showing the dominant role of SSH. Besides, the upper-layer (0–300 m) transports across the Luzon Strait (120.78°E, 18.5°N-22°N) are estimated at 0.27 Sv in December 1996, −7.25 Sv in December 1997, and −2.17 Sv in December 1998. As stronger Luzon Strait transport has been linked to lower NWL-SLA in the literature (Zheng et al., 2007; Wu, 2013), the estimated LST seems to correspond to the NWL-SSH changes from the El Niño year of 1997 to the La Niña year of 1998. However, the mismatched NWL-SSH ranking yielded by the WyyBcdEyy-UVST experiments, in which only time-varying SSHs were excluded at the eastern boundary of SCSM, rules out the LST as the primary controlling factor (Fig. 10). That is, the super-ENSO-related NWL-SSH changes are driven by super-ENSO-induced wave motions in the tropical western Pacific, rather than ocean currents.

Further, we divided the total SSH in the CTL into barotropic (SSHbt) and baroclinic (SSHbc) components. Following the definition of steric sea level derived from interior density anomalies (McWilliams et al., 2024; Storto et al., 2019), the baroclinic component is calculated as follows:

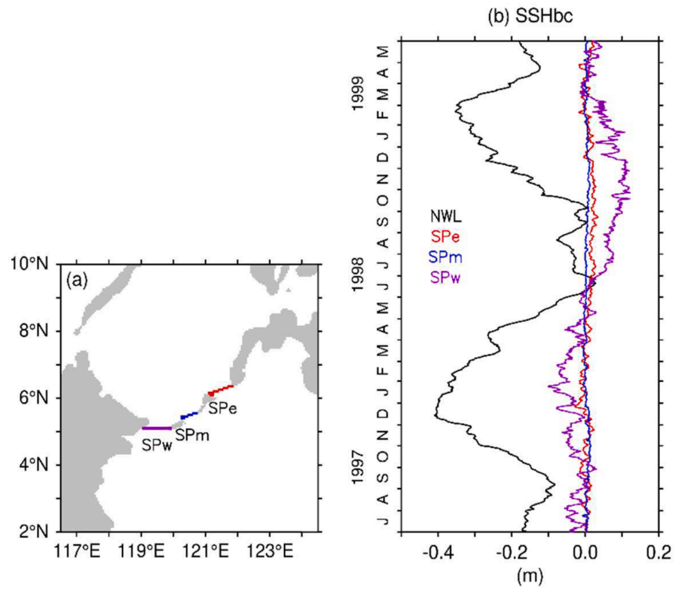

Fig. 13. (a) SPe, SPm, and SPw denote the three main gaps in the Sibutu Passage. (b) Time series of SSHbc (unit: m) at the three main gaps (SPe, SPm, SPw) of Sibutu Passage and NWL-SSHbc for the 1997–1998 super ENSO.

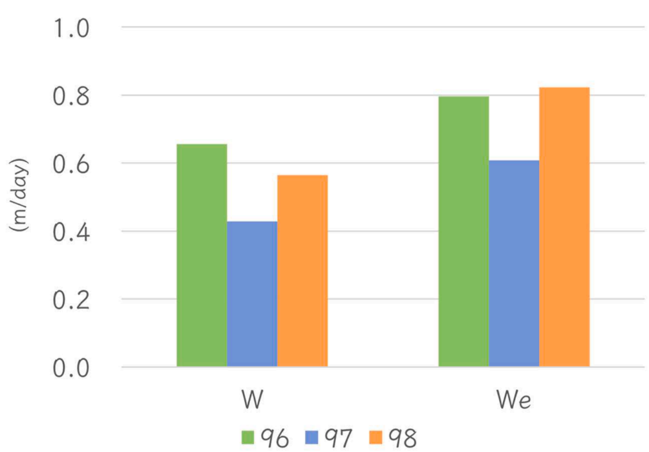

Fig. 14. The depth-averaged (0–50 m) vertical velocity (unit: m/day) and wind stress curl induced Ekman pumping velocity ($w_e = WSC/\rho_0 f = 1.54 \times 10^6 \times WSC$; unit: m/day) averaged over the NWL for the 1996–1998.

$$SSH_{bc} = \int_{-H}^{0} \frac{\overline{\rho}(z) - \rho(x, y, z, t)}{\rho_0} dz \tag{1}$$

where H is the water depth, $\overline{\rho}(z)$ represents the reference background density profile, $\rho(x, y, z, t)$ is the simulated seawater density, and ρ_0=1025 kg/m^3 is the reference seawater density.

Subsequently, the barotropic component, which primarily reflects the ocean bottom pressure variations, is obtained by subtracting the baroclinic contribution from the SSH:

$$SSH_{bt} = SSH - SSH_{bc} \tag{2}$$

Based on the CTL simulation, the order of middle-low-high was observed in NWL-SSHbc for both super ENSO of 1997–1998 and 2015–2016, but this order was absent in NWL-SSHbt (Fig. 11 and Figure S6). Furthermore, the SSHbc in both the NWL and the tropical western Pacific (TWP; 128°E-130°E, 3°N-17°N) exhibits a consistent middle-low-high pattern, implying that super-ENSO-related NWL-SLA could originate from the baroclinic sea level changes in the TWP, rather than the barotropic sea level changes. This is also supported by applying the time-varying baroclinic component of SSH at the eastern boundary of the SCSM (WyyBcdEyy-SSHbc), in which the experiment successfully reproduces the NWL-SSH ranking of medium, low, high (Fig. 10).

Sequentially, Fig. 12c and d track the SSHbc from the TWP to NWL along the blue and purple routes shown in Fig. 12a and b, respectively, to examine the pathway of baroclinic wave motion. The SSHbc propagated westward at a speed of 15–16 km/day from TWP to EP and accelerated along the blue route from EP to NWL at a speed of 180–225 km/day; then, it continued moving from NWL back to EP along the purple route at a slower speed of 150–180 km/day, forming a clockwise cycle. The propagation speed during the first stage corresponds with the typical first-mode baroclinic Rossby wave speed (Chelton and Schlax, 1996) and those during the latter two stages are consistent with the typical baroclinic coastal Kelvin wave speed (Brink, 1982). It is noteworthy that the propagation speeds of baroclinic waves during 1998 were faster than those during 1997. This is due to the greater reduced gravity (g') associated with the stronger stratification during 1998, the La Niña year, in the tropical western Pacific. The result evidences that upwelling (downwelling) baroclinic Rossby waves associated with negative (positive) SLAs propagate westward during El Niño (La Niña) years. After impinging on the Philippine coast, they transform into coastal trapped waves, propagate clockwise along the coast, arrive at the northern SCS, and finally regulate the SSH in the NWL.

Because there are three main gaps in the Sibutu Passage (SPe, SPm, and SPw; Fig. 13a), we further compare the time series of SSHbc at the three gaps with NWL-SSHbc. The magnitude of SSHbc in the SPw is significantly greater than the other two (Fig. 13b), showing that the SPw acts as the primary pathway for wave propagation whereas waves in the other two channels dissipate rapidly due to their shallow depths.

5. Discussions

In this study, we have examined the super-ENSO-related sea level changes in the NWL and explored the mechanism regulating the NWL-SLA during super ENSO. Since sea level changes are always tied to upwelling intensity changes, which greatly influence the surrounding biogeochemical distribution, changes in NWL vertical velocity, which directly reflects the upwelling intensity, during the two super ENSO of 1997–1998 and 2015–2016 are further examined (Fig. 14 and S7). We found that changes in vertical velocity show orders of large-small-middle for the 1997–1998 super ENSO and middle-small-large for the 2015–2016 super ENSO, which do not align with the order of middle-low-high for NWL-SLA. In other words, the sea level change is not a reliable indicator to reflect the upwelling intensity change in the NWL during super ENSO. Instead, the vertical velocity change shows a good consistency with the change in WSC-induced Ekman pumping velocity. This scale-decoupling process off northwestern Luzon mirrors the broader event-to-event differences across the SCS during the 1997/1998 and 2015/2016 super ENSO cycles, which manifested as extreme basin-scale warming (Xiao et al., 2020a) and non-uniform coastal upwelling responses (Xiao et al., 2020c).

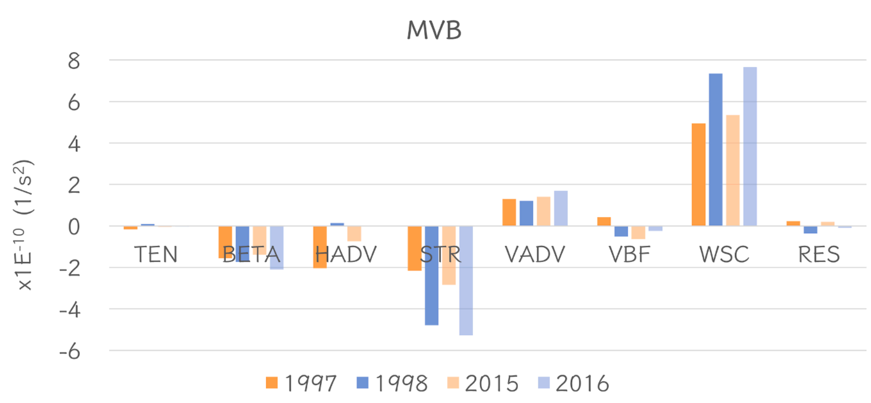

Fig. 15. Vertically integrated relative vorticity budget within the ocean mixed layer (MVB) during 1997–1998 and 2015–2016 super ENSO. Individual terms represent the local tendency (TEN), planetary β-effect (BETA), horizontal advection (HADV), vortex stretching (STR), vertical advection (VADV), vertical boundary flux (VBF), surface wind stress curl (WSC), and the residual/dissipation (RES). Unit is $1/s^2$.

Further, relative vorticity budget within the ocean mixed layer (MVB) is adopted to explain the inconsistency between NWL-SLA and vertical velocity during super ENSO. The vertically integrated relative vorticity equation (e.g., Gan et al., 2016; Wang et al., 2023) over the mixed layer is diagnosed as follows:

$$\underbrace{\left\langle \frac{\partial\widetilde{\zeta}}{\partial t}\right\rangle}_{TEN} = \underbrace{\langle -\beta\widetilde{v}\rangle}_{BETA} + \underbrace{\langle -(\widetilde{\mathbf{U}\cdot\nabla\zeta})\rangle}_{HADV} + \underbrace{\langle -((\widetilde{\zeta+f})\nabla\cdot\mathbf{U})\rangle}_{STR} + \underbrace{\left\langle -\left(\widetilde{w\frac{\partial\zeta}{\partial z}}\right)\right\rangle}_{VADV} + \underbrace{\langle \zeta|_{-h}w_e\rangle}_{VBF} + \underbrace{\left\langle \frac{1}{\rho_0}(\nabla\times\boldsymbol{\tau})_z\right\rangle}_{WSC} + \underbrace{\langle\widetilde{\mathscr{R}}\rangle}_{RES} \quad (3)$$

where the tilde ($\sim$) denotes a vertical integral from the sea surface ($z = 0$) to the climatological monthly mixed layer base ($z = -h_{MLD}(x,y,m)$), and the angle brackets ($\langle\cdot\rangle$) denote the horizontal spatial average over the NWL area. The velocity and vorticity fields are evaluated from daily snapshots of the CTL, while the integration depth is determined from the climatological monthly mixed layer depth. The relative vorticity is defined as $\zeta = (\nabla \times \mathbf{U})_z = \partial v/\partial x - \partial u/\partial y$, where $\mathbf{U} = (u, v)$ denotes the horizontal velocity vector, w is the vertical velocity. w_e represents the effective cross-boundary velocity across the mixed layer base, including the vertical velocity and the horizontal advection across the sloping mixed layer boundary ($w_e > 0$ denotes into the mixed layer). Additionally, the meridional gradient of the Coriolis parameter f is given by $\beta = \partial f/\partial y$, and ρ_0 is the reference seawater density. Finally, $\boldsymbol{\tau}$ is the sea surface wind stress vector, and $\mathscr{R}$ encapsulates the residual forces, unresolved subgrid-scale processes, and the unresolved stress curl at the integration boundary.

As revealed in Fig. 15, the WSC and the stretching term (STR) constitute the leading order balance within the mixed layer. Besides, the magnitudes of WSC and STR far exceed those of the horizontal advection (HADV) and the planetary β-effect (BETA). This distinct balance provides a rigorous explanation for the strong coupling between the wind field and the vertical motion. The positive WSC physically drives an upward Ekman pumping velocity at the base of the mixed layer. As this vertical motion attenuates through the shallow mixed layer, it induces a significant vertical velocity gradient ($\partial w/\partial z$), which is instantaneously converted into intense negative vortex stretching (STR). Furthermore, the MVB reveals that the TEN remains negligibly small across all analyzed years, despite the massive opposing forces of WSC and STR. In fluid dynamics, this near-zero tendency indicates that the mixed layer maintains a rapid, quasi-steady geostrophic adjustment. Rather than accumulating vorticity locally over time, the intense fluid convergence or divergence driven by the episodic wind events is efficiently balanced by the stretching term on synoptic timescales. Consequently, the local relative vorticity evolution and the vertical motion are dynamically locked together, functioning as a direct, real-time response to the prevailing wind stress curl anomalies over the NWL.

The MVB analysis highlights that Horizontal Advection (HADV) and the Beta Effect (BETA) within the mixed layer are negligible compared to WSC and STR. This is the crucial point for explaining the inconsistency with total/baroclinic SLA. Total SLA and baroclinic SLA in the NWL during super ENSO are heavily weighted by the baroclinic mode, which depends on the slow, large-scale advection of density and the displacement of the deep thermocline far below the mixed layer. Within the mixed layer, a strong wind event can instantly stir up WSC, trigger and deform the free surface within days. However, this high-frequency energy is confined to the mixed layer and the fast-propagating barotropic mode. The deep baroclinic thermocline, which possesses massive available potential energy (APE), remains undisturbed by these transient mixed-layer budget fluctuations. Because the mixed layer dynamics are inherently high-frequency and decoupled from the slow, high-inertia advective adjustments (HADV/BETA) of the deep thermocline, the system exhibits a classic scale-decoupled state. Thus, the transient drivers within the mixed layer (WSC ≈ w ≈ STR) are perfectly phase-locked, yet they remain collectively independent of the total/baroclinic SSH field.

6. Conclusions

Previous studies documented that low SLA off the northwestern coast of Luzon (NWL-SLA) in the South China Sea (SCS) were unusually elevated during winter 1998, when a super La Niña occurred following the strongest El Niño of the 20th century. The present study first examined satellite remote sensing December sea-level data to determine whether the low NWL-SLA consistently respond to both the 1997/1998 and 2015/2016 super ENSO. Our analysis reveals that December mean NWL-SLA rank as medium during normal pre-El Niño years, low during El Niño years, and high during La Niña years in both events. This super-ENSO-related pattern was successfully reproduced by the control simulation of the well-validated three-dimensional SCSM, which incorporated realistic bottom topography, surface heat and momentum fluxes based on atmospheric reanalysis, and lateral boundary conditions derived from HyCOM data assimilation products.

Using the well-validated SCSM, we conducted a series of numerical experiments to systematically elucidate the dynamical processes driving low NWL-SLA genesis and its super-ENSO-related variations. Our findings demonstrate that local positive WSC off northwestern Luzon serves as the primary generator of low NWL-SLA during winter, rather than SCS basin-scale circulation or remote forcing from outside the basin. However, the NWL sea-level changes are controlled by remote signals in the tropical Pacific Ocean during super ENSO, but not the local positive WSC changes or ocean current variability near the Luzon Strait. We further clarify that these remote signals are contributed by the baroclinic component of SLA and propagate westward as baroclinic Rossby waves in the tropical western Pacific, then transform into baroclinic coastal Kelvin waves upon reaching the Philippine coast, and enter the SCS clockwise through the southernmost gap of Sibutu Passage and Mindoro Strait. Furthermore, since strengthened stratification in the tropical western Pacific during La Niña years amplifies the reduced gravity, the propagation of baroclinic waves accelerates relative to El Niño years.

Besides, the interannual variability of vertical velocity is found to misalign with the NWL-SLA during super ENSO, implying that the sea level change is not a reliable indicator to reflect upwelling intensity change for a super ENSO cycle from a normal pre-El Niño year to a La Niña year. The deviation between NWL-SLA and vertical velocity during super ENSO highlights a scale-decoupling between the mixed layer and deep ocean. While vertical velocity acts as a high-frequency response to wind stress curl, the SLA is determined by the low-frequency advective adjustments of the deep thermocline, which remains unperturbed by transient mixed-layer budget fluctuations.

This study advances our understanding of how the wintertime low NWL-SLA responds to super ENSO and elucidates the underlying dynamical mechanisms driving these responses.

CRediT authorship contribution statement

Tzu-Ling Chiang: Writing – original draft, Visualization, Validation, Methodology, Investigation, Formal analysis, Data curation, Conceptualization. **Yi-Chia Hsin:** Writing – review & editing, Visualization, Validation, Supervision, Formal analysis. **Chau-Ron Wu:** Writing – review & editing, Supervision, Resources, Funding acquisition, Conceptualization.

Declaration of competing interest

The authors declare that they have no known competing financial interests or personal relationships that could have appeared to influence the work reported in this paper.

Acknowledgments

This research was supported by the Academia Sinica, under grants AS-GCP-112-M02 and AS-KPQ-112-NETZ-03, and National Science and Technology Council, Taiwan, ROC, under grants NSTC 113-2611-M-003-003 NSTC 114-2611-M-001-003 and NSTC 114-2611-M-003-001. We would like to thank the Copernicus Marine Service (CMEMS; https://marine.copernicus.eu/) for the 0.125° Data Unification and Altimeter Combination System (DUACS) altimeter gridded sea surface height dataset, the Copernicus Climate Change Service (C3S; https://climate.copernicus.eu/) for the 0.25° fifth generation European Centre for Medium-Range Weather Forecasts (ECMWF) atmospheric reanalysis (ERA5) of the global climate, and the global Hybrid Coordinate Ocean Model (HyCOM; https://www.hycom.org) for the 1/12° model simulations.

Supplementary materials

Supplementary material associated with this article can be found, in the online version, at doi:10.1016/j.ocemod.2026.102817.

Data availability

The Data Unification and Altimeter Combination System (DUACS) altimeter gridded sea surface height dataset used during this study is openly available from Copernicus Marine Service at https://doi.org/10.48670/moi-00148. The fifth generation European Centre for Medium-Range Weather Forecasts (ECMWF) atmospheric reanalysis (ERA5) of the global climate from Copernicus Climate Change Service at https://doi.org/10.24381/cds.adbb2d47. The model simulations from the global Hybrid Coordinate Ocean Model (HyCOM) are available at https://www.hycom.org/.

References

Bouma, M.J., Kovats, R.S., Goubet, S.A., Cox, J.S.H., Haines, A., 1997. Global assessment of El Niño's disaster burden. Lancet 350 (9089), 1435–1438. https://doi.org/10.1016/s0140-6736(97)04509-1.

Brink, K.H., 1982. A comparison of long coastal trapped wave theory with observations off Peru. J. Phys. Oceanogr. 12 (8), 897–913. https://doi.org/10.1175/1520-0485(1982)012%3C0897:ACOLCT%3E2.0.CO;2.

Chao, S.-Y., Shaw, P.-T., Wu, S.Y., 1996. El Niño modulation of the South China sea circulation. Prog. Oceanogr. 38 (1), 51–93. https://doi.org/10.1016/S0079-6611(96)00010-9.

Chelton, D.B., Schlax, M.G., 1996. Global observations of oceanic Rossby waves. Science 272 (5259), 234–238. https://doi.org/10.1126/science.272.5259.234.

Chen, D., Lian, T., Fu, C., Cane, M.A., Tang, Y., Murtugudde, R., Song, X., Wu, Q., Zhou, L., 2015. Strong influence of westerly wind bursts on El Niño diversity. Nat. Geosci. 8, 339–345. https://doi.org/10.1038/ngeo2399.

Chen, L., Li, T., Wang, B., Wang, L., 2017. Formation mechanism for 2015/16 super El Niño. Sci. Rep. 7, 2975. https://doi.org/10.1038/s41598-017-02926-3.

Chiang, T.-L., Wu, C.-R, Chao, S.-Y., 2008. Physical and geographical origins of the South China sea warm current. J. Geophys. Res.: Oceans 113 (C8), C08028. https://doi.org/10.1029/2008JC004794.

Chiang, T.-L., Wu, C.-R., Oey, L.-Y., 2011. Typhoon Kai-Tak: an ocean's perfect storm. J. Phys. Oceanogr. 41 (1), 221–233. https://doi.org/10.1175/2010JPO4518.1.

Chu, P.C., Chen, Y., Lu, S., 1998. Wind-driven South China sea deep basin warm-core/cool-core eddies. J. Oceanogr. 54, 347–360. https://doi.org/10.1007/BF02742619.

Copernicus Climate Change Service (C3S), 2017. ERA5: Fifth generation of ECMWF Atmospheric Reanalyses of the Global Climate. Copernicus Climate Change Service Climate Data Store (CDS). https://cds.climate.copernicus.eu/.

Gan, J., Liu, Z., Hu, C.R., 2016. A three-layer alternating spinning circulation in the South China sea. J. Phys. Oceanogr. 46 (8), 2309–2315. https://doi.org/10.1175/JPO-D-16-0044.1.

Hersbach, H., Bell, B., Berrisford, P., Hirahara, S., Horányi, A., Muñoz-Sabater, J., Nicolas, J., Peubey, C., Radu, R., Schepers, D., Simmons, A., Soci, C., Abdalla, S., Abellan, X., Balsamo, G., Bechtold, P., Biavati, G., Bidlot, J., Bonavita, M., Chiara, G. D., Dahlgren, P., Dee, D., Diamantakis, M., Dragani, R., Flemming, J., Forbes, R., Fuentes, M., Geer, A., Haimberger, L., Healy, S., Hogan, R.J., Hólm, E., Janisková, M., Keeley, S., Laloyaux, P., Lopez, P., Lupu, C., Radnoti, G., Rosnay, P.D., Rozum, I., Vamborg, F., Villaume, S., Thépaut, J., 2020. The ERA5 global reanalysis. Q. J. R. Meteorol. Soc. 146 (730), 1999–2049. https://doi.org/10.1002/qj.3803.

Hein, H., Hein, B., Pohlmann, T., Long, B., 2013. Inter-annual variability of upwelling off the South-Vietnamese coast and its relation to nutrient dynamics. Glob. Planet. Change 110 (B), 170–182. https://doi.org/10.1016/j.gloplacha.2013.09.009.

Hu, J., Wang, X.H., 2016. Progress on upwelling studies in the China seas. Rev. Geophys. 54 (3). https://doi.org/10.1002/2015RG000505.

Isoguchi, O., Kawamura, H., 2006. MJO-related summer cooling and phytoplankton blooms in the South China sea in recent years. Geophys. Res. Lett. 33 (16). https://doi.org/10.1029/2006GL027046.

Kämpf, J., Chapman, P., 2016. Upwelling Systems of the World. Springer International Publishing Switzerland, p. 433. https://doi.org/10.1007/978-3-319-42524-5.

Li, M., Xue, H., Wei, J., Liang, L., Gordon, A.L., Yang, S., 2021. The role of the mindoro-sibutu pathway on the South China sea multilayer circulation. J. Phys. Oceanogr. 51 (9), 2767–2782. https://doi.org/10.1175/JPO-D-20-0165.1.

Liu, K.-K., Chao, S.-Y., Shaw, P.-T., Gong, G.-C., Chen, C.-C., Tang, T.Y., 2002. Monsoon-forced chlorophyll distribution and primary production in the South China sea: observations and a numerical study. Oceanogr. Res. Pap. 49 (8), 1387–1412. https://doi.org/10.1016/S0967-0637(02)00035-3.

Liu, Q., Kaneko, A., Su, J., 2008. Recent progress in studies of the South China sea circulation. J. Oceanogr. 64, 753–762. https://doi.org/10.1007/s10872-008-0063-8.

Lu, W., Yan, X.-H., Jiang, Y., 2015. Winter bloom and associated upwelling northwest of the Luzon Island: a coupled physical-biological modeling approach. J. Geophys. Res.: Oceans 120 (1), 533–546. https://doi.org/10.1002/2014JC010218.

Martin, M.C., Villanoy, C.L., 2007. Sea surface variability of upwelling area northwest of Luzon, Philippines. Dynamic Planet. In: Tregoning, P., Rizos, C. (Eds.), International Association of Geodesy Symposia, International Association of Geodesy Symposia, 130. Springer, Berlin, Heidelberg. https://doi.org/10.1007/978-3-540-49350-1_15.

McWilliams, J.C., Molemaker, M.J., Damien, P., 2024. Baroclinic sea level. J. Adv. Model. Earth Syst. 16 (4), e2023MS003977. https://doi.org/10.1029/2023MS003977.

McPhaden, M.J., Zebiak, S.E., Glantz, M.H., 2006. ENSO as an integrating concept in earth science. Science 314 (5806), 1740–1745. https://doi.org/10.1126/science.1132588.

Mellor, G.L., 2004. Users guide for a three-dimensional, primitive equation, numerical ocean model. Program Atmos. Ocean. Sci. 56.

Ngo, M.-H., Hsin, Y.-C., 2021. Impacts of wind and current on the interannual variation of the summertime upwelling off southern Vietnam in the South China sea. J. Geophys. Res.-Oceans 126 (6), e2020JC016892. https://doi.org/10.1029/2020JC016892.

Ngo, M.-H., Hsin, Y.-C., 2024. Three-dimensional structure of temperature, salinity, and velocity of the summertime vietnamese upwelling system in the South China sea on the interannual timescale. Prog. Oceanogr. 229, 103354. https://doi.org/10.1016/j.pocean.2024.103354.

Qu, T., 2000. Upper-layer circulation in the South China sea. J. Phys. Oceanogr. 30 (6), 1450–1460. https://doi.org/10.1175/1520-0485(2000)030<1450:ULCITS>2.0.CO;2.

Santoso, A., McPhaden, M.J., Cai, W., 2017. The defining characteristics of ENSO extremes and the strong 2015/2016 El Niño. Rev. Geophys. 55 (4), 1079–1129. https://doi.org/10.1002/2017RG000560.

Shaw, P.T., Chao, S.-Y., 1994. Surface circulation in the South China sea. Oceanogr. Res. Pap. 41 (11–12), 1663–1683. https://doi.org/10.1016/0967-0637(94)90067-1.

Shaw, P.-T., Chao, S.-Y., Fu, L.-L., 1999. Sea surface height variations in the South China sea from satellite altimetry. Oceanol. Acta 22 (1), 1–17. https://doi.org/10.1016/S0399-1784(99)80028-0.

Shaw, P.-T., Chao, S.-Y., Liu, K.-K., Pai, S.-C., Liu, C.-T., 1996. Winter upwelling off Luzon in the northeastern South China sea. J. Geophys. Res. 101 (C7), 16435–16448. https://doi.org/10.1029/96JC01064.

Storto, A., Bonaduce, A., Feng, X., Yang, C., 2019. Steric sea level changes from ocean reanalyses at global and regional scales. Water 11 (10), 1987. https://doi.org/10.3390/w11101987.

Umasangaji, H., Ramili, Y., 2021. Mini review: characteristics of upwelling in several coastal areas in the world. Earth Environ. Sci. 890, 012004. https://doi.org/10.1088/1755-1315/890/1/012004.

Voss, M., Bombar, D., Loick, N., Dippner, J.W., 2006. Riverine influence on nitrogen fixation in the upwelling region off Vietnam, South China sea. Geophys. Res. Lett. 33 (7), L07604. https://doi.org/10.1029/2005GL025569.

Wang, J., Tang, D., Sui, Y., 2010. Winter phytoplankton bloom induced by subsurface upwelling and mixed layer entrainment southwest of Luzon Strait. J. Mar. Syst. 83 (3–4), 141–149. https://doi.org/10.1016/j.jmarsys.2010.05.006.

Wang, Q., Zeng, L., Chen, J., He, Y., Liu, Q., Sui, D., Wang, D., 2023. Phase shift of the winter South China sea western boundary current over the past two decades and its drivers. Geophys. Res. Lett. 50 (10), e2023GL103145. https://doi.org/10.1029/2023GL103145.

Wu, C.-R., 2013. Interannual modulation of the pacific decadal oscillation (PDO) on the low-latitude western North Pacific. Prog. Oceanogr. 110, 49–58. https://doi.org/10.1016/j.pocean.2012.12.001.

Wu, C.-R., Chang, C.-W.J., 2005. Interannual variability of the South China sea in a data assimilation model. Geophys. Res. Lett. 32 (17), L17611. https://doi.org/10.1029/2005GL023798.

Wu, C.-R., Chiang, T.-L., 2007. Mesoscale eddies in the northern South China sea. Deep Sea Res. II: Trop. Stud. Oceanogr. 54 (14–15), 1575–1588. https://doi.org/10.1016/j.dsr2.2007.05.008.

Wu, C.-R., Shaw, P.-T., Chao, S.-Y., 1998. Seasonal and interannual variations in the velocity field of the South China sea. J. Oceanogr. 54, 361–372. https://doi.org/10.1007/BF02742620.

Xiao, F., Zeng, L., Liu, Q., Zhou, W., Wang, D., 2018. Extreme subsurface warm events in the South China sea during 1998/99 and 2006/07: observations and mechanisms. Clim. Dyn. 50, 115–128. https://doi.org/10.1007/s00382-017-3588-y.

Xiao, F., Wang, D., Zeng, L., Liu, Q., Zhou, W., 2019. Contrasting changes in the sea surface temperature and upper ocean heat content in the South China sea during recent decades. Clim. Dyn. 53, 1597–1612. https://doi.org/10.1007/s00382-019-04697-1.

Xiao, F., Wang, D., Leung, M.Y.T., 2020a. Early and extreme warming in the South China sea during 2015/16: role of an unusual Indian Ocean dipole event. Geophys. Res. Lett. 47 (17), e2020GL089936. https://doi.org/10.1029/2020GL089936.

Xiao, F., Wang, D., Yang, L., 2020b. Can tropical pacific winds enhance the footprint of the interdecadal pacific oscillation on the upper-ocean heat content in the South China sea? J. Clim. 33 (10), 4419–4437. https://doi.org/10.1175/JCLI-D-19-0679.1.

Xiao, F., Wu, Z., Lyu, Y., Zhang, Y., 2020c. Abnormal strong upwelling off the coast of southeast Vietnam in the late summer of 2016: a comparison with the case in 1998. Atmosphere 11 (9), 940. https://doi.org/10.3390/atmos11090940.

Xie, S.-P., Xie, Q., Wang, D., Liu, W.T., 2003. Summer upwelling in the South China sea and its role in regional climate variations. J. Geophys. Res. 108 (C8), 3261. https://doi.org/10.1029/2003JC001867.

Zhao, H., Tang, D.L., 2007. Effect of 1998 El Niño on the distribution of phytoplankton in the South China sea. J. Geophys. Res.: Oceans 112 (C2), C02017. https://doi.org/10.1029/2006jc003536.

Zheng, Z.-W., Ho, C.-R., Kuo, N.-J., 2007. Mechanism of weakening of west Luzon eddy during La Niña years. Geophys. Res. Lett. 34 (11). https://doi.org/10.1029/2007gl030058.

Zhuang, W., Qiu, B., Du, Y., 2013. Low-frequency western pacific ocean sea level and circulation changes due to the connectivity of the philippine archipelago. J. Geophys. Res. 118 (12), 6759–6773. https://doi.org/10.1002/2013jc009376.